Nano-Micro Letters

e-ISSN 2150-5551
CN 31-2103/TB

ARTICLE

https://doi.org/10.1007/s40820-025-01770-9

Cite as
Nano-Micro Lett.
(2025) 17:276

Received: 28 January 2025
Accepted: 16 April 2025
© The Author(s) 2025

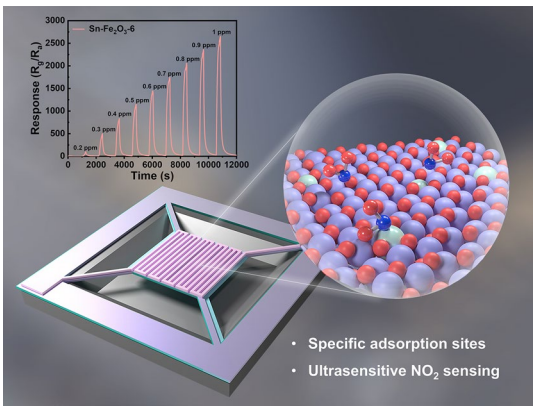
Specific Sn–O–Fe Active Sites from Atomically Sn-Doping Porous Fe_2O_3 for Ultrasensitive NO_2 Detection

Yihong Zhong[1], Guotao Yuan[2], Dequan Bao[3], Yi Tao[1], Zhenqiu Gao[1], Wei Zhao[1], Shuo Li[1], Yuting Yang[1], Pingping Zhang[4,5], Hao Zhang[1] ✉, Xuhui Sun[1] ✉

HIGHLIGHTS

- The heteroatom atomically doping strategy was reported to construct highlyefficient sites on metal oxides for the detection of low-concentration gas.
- The atomically dispersed Sn atoms were intentionally incorporated into the Fe_2O_3lattice during the oxidative annealing of Fe-based metal organic framework,leading to specific Sn–O–Fe sites, porous structures, and abundant oxygenvacancies.
- The optimized Sn-Fe_2O_3 exhibited exceptional sensing performance for NO_2detection: ultra-high sensitivity (*Rg*/*Ra*=2646.6 to 1 ppm NO_2), ultra-low limit ofdetection (10 ppb), and high selectivity.

ABSTRACT Conventional gas sensing materials (e.g., metal oxides) suffer from deficient sensitivity and serve cross-sensitivity issues due to the lack of efficient adsorption sites. Herein, the heteroatom atomically doping strategy is demonstrated to significantly enhance the sensing performance of metal oxides-based gas sensing materials. Specifically, the Sn atoms were incorporated into porous Fe_2O_3 in the form of atomically dispersed sites. As revealed by X-ray absorption spectroscopy and atomic-resolution scanning transmission electron microscopy, these Sn atoms successfully occupy the Fe sites in the Fe_2O_3 lattice, forming the unique Sn–O–Fe sites. Compared to Fe–O–Fe sites (from bare Fe_2O_3) and Sn–O–Sn sites (from SnO_2/Fe_2O_3 with high Sn loading), the Sn–O–Fe sites on porous Fe_2O_3 exhibit a superior sensitivity (R_g/R_a = 2646.6) to 1 ppm NO_2, along with dramatically increased selectivity and ultra-low limits of detection (10 ppb). Further theoretical calculations suggest that the strong adsorption of NO_2 on Sn–O–Fe sites (N atom on Sn site, O atom on Fe site) contributes a more efficient gas response, compared to NO_2 on Fe–O–Fe sites and other gases on Sn–O–Fe sites. Moreover, the incorporated Sn atoms reduce the bandgap of Fe_2O_3, not only facilitating the electron release but also increasing the NO_2 adsorption at a low working temperature (150 °C). This work introduces an effective strategy to construct effective adsorption sites that show a unique response to specific gas molecules, potentially promoting the rational design of atomically modified gas sensing materials with high sensitivity and high selectivity.



KEYWORDS Atomically doping; Specific Sn–O–Fe sites; NO_2 detection; Gas sensor; Specific adsorption

✉ Hao Zhang, haozhang@suda.edu.cn; Xuhui Sun, xhsun@suda.edu.cn
[1] Institute of Functional Nano and Soft Materials (FUNSOM), Jiangsu Key Laboratory for Carbon-Based Functional Materials and Devices Jiangsu Key Laboratory of Advanced Negative Carbon Technologies, Soochow University, Suzhou 215123, People's Republic of China
[2] College of Chemistry and Environmental Engineering, Shenzhen University, Shenzhen 518060, People's Republic of China
[3] The Key Laboratory of Rare Earth Functional Materials and Applications, Zhoukou Normal University, Zhoukou 466000, People's Republic of China
[4] Suzhou Huiwen Nanotechnology Co., Ltd., Suzhou 215000, People's Republic of China
[5] Materials Science Gusu Laboratory, Suzhou 215123, China

Published online: 26 May 2025

Shanghai Jiao Tong University Press

Springer

1 Introduction

In contemporary industrial production and residential life, the timely monitoring of particular gases is of paramount importance [1–6]. As one of the most hazardous gases, nitrogen dioxide (NO_2) could cause serious respiratory diseases even in a trace amount [7, 8]. The World Health Organization recommends that NO_2 concentration in the environment should not exceed 82 ppb, highlighting the importance of monitoring low-concentration NO_2 [9]. Generally, metal oxide semiconductors (MOS) have been widely used as gas sensing material owing to their comprehensive features, such as semiconducting character, nontoxicity, abundance, and chemical stability [10, 11]. However, most MOS-based gas sensors for NO_2 detection have to operate at a high temperature (> 200 °C) and exhibit limited response and selectivity [12]. The unsatisfactory performance is mainly due to the lack of effective adsorption sites on metal oxides, and the cross-sensitivity issues would become more severe for low-concentration gas detection. Therefore, constructing highly efficient adsorption sites on MOS is of great significance to realize the detection of low-concentration NO_2.

Recently, single-atom catalysts (SACs) featuring maximum atomic efficiency have attracted extensive attention in (electro)catalysis fields, in which the atomically dispersed sites with specific active structures present unprecedented catalytic performance [13–17]. Compared to nanoparticles or nanoclusters, SAC can maximally expose the active centers to boost the reaction efficiency [18]. Considering that the gas sensing process resembles surface catalysis, the atomically dispersed sites from SACs are expected to offer excellent gas sensing performance. For example, Gu et al. prepared Pt SAC on WO_3 using the template method, in which the atomically dispersed Pt with high activity showed exceptional response toward triethylamine [19]. Feng et al. designed the SnO_2 nanospheres functionalized by Au SAC, resulting in a Listeria monocytogene sensor with high sensitivity and selectivity [20]. In addition, Wang et al. constructed Cu SAC as catalytic sites on $WO_{2.72}$ nanowires (Cu SAC/$WO_{2.72}$) for the detection of toluene [21]. The atomically dispersed Cu sites contributed to a strong affinity toward toluene and a lowered reaction barrier. The above works demonstrate that the atomically dispersed sites can significantly enhance the gas sensing performance of MOS-based gas sensors [22, 23]. Notably, directly incorporating atomically dispersed sites onto the surface of metal oxides might produce various active sites with multiple coordination environments, unavoidably altering the adsorption strength of gas molecules and reducing the sensing selectivity of corresponding sensors. Therefore, precisely controlling the location of atomically dispersed sites in metal oxides is essential to ensuring the structural uniformity of exposed active sites but remains challenging.

In this work, atomically dispersed Sn atoms were incorporated into the Fe_2O_3 lattice, which offers highly efficient sites for the detection of low-concentration NO_2. Firstly, the ligands in Fe-based metal organic framework (MOF) are utilized as the fences to spatially separate these Sn atoms. During the following annealing process, Fe-based MOF transforms into porous Fe_2O_3; meanwhile, Sn atoms enter into the Fe_2O_3 lattice and occupy the lattice sites of Fe atoms, leading to the formation of Sn–O–Fe sites. The specific coordination environments of the Sn–O–Fe sites have been verified by high-angle annular dark-field scanning transmission electron microscopy (HAADF-STEM) and synchrotron-based X-ray absorption spectroscopy (XAS) measurements. The incorporated Sn atoms not only regulate the energy band structure of α-Fe_2O_3 but also enhance specific adsorption to NO_2 molecules. Additionally, the obtained Fe_2O_3 possesses a mesoporous structure and abundant oxygen vacancies, both of which are conducive to the gas sensing process. As a result, the optimized sample (Sn–Fe_2O_3–6) exhibits extraordinary sensing response to NO_2 ($R = 2646.6$ to 1 ppm NO_2 at 150 °C), ultra-low detection limit (10 ppb), and excellent selectivity.

2 Experimental Section

2.1 Reagents and Materials

Pluronic F-127 ($EO_{97}PO_{69}EO_{97}$, with an average $M_n = 12{,}600$) is obtained from Sigma-Aldrich. Iron chloride hexahydrate ($FeCl_3{\cdot}6H_2O$, 99%), stannic chloride pentahydrate ($SnCl_4{\cdot}5H_2O$, 99%), 2-aminoterephthalic acid (H_2N-BDC, 99%), and acetic acid (CH_3COOH, 99.7%) were obtained Shanghai Aladdin Biochemical Technology Co., Ltd. All chemicals were used as received without undergoing an additional purification process.

© The authors
https://doi.org/10.1007/s40820-025-01770-9

2.2 Synthesis of Sn-Fe_2O_3

2.2.1 Fe-MIL-88B-NH_2-Sn-X Precursors

The Fe-MOF was prepared by a hydrothermal method based on the previous work with some modifications [24]. Typically, 0.32 g of Pluronic F-127 was dissolved in 26.7 mL of deionized water and stirred for 2 h. Next, 3.3 mL of $FeCl_3 \cdot 6H_2O$ (0.4 M) was added to the surfactant solution. The resulting mixture was stirred for 1.5 h before injecting 0.6 mL of acetic acid. After stirring for 1.5 h, 120 mg of 2-aminoterephthalic acid was added and stirred for an additional 2 h. The resulting resolution was then transferred into a 50 mL Teflon-lined stainless steel autoclave and heated at 110 °C for 24 h. After cooling to room temperature, the dark brown powders were collected by centrifugation and purified with ethanol three times. Finally, the as-synthesized Fe-MOF denoted as Fe-MIL-88B-NH_2-Sn-0 was dried overnight in a vacuum dryer at 60 °C. The Fe-MIL-88B-NH_2-Sn-X ($X = 2, 4, 6, 8$) was synthesized using the same method as before, with the addition of $SnCl_4 \cdot 5H_2O$ to the surfactant solution while adding $FeCl_3 \cdot 6H_2O$. The molar ratios of Sn ions to Fe ions were set as 2%, 4%, 6%, and 8%, denoted as Fe-MIL-88B-NH_2-Sn-2, Fe-MIL-88B-NH_2-Sn-4, MIL-88B-NH_2-Sn-6, and Fe-MIL-88B-NH_2-Sn-8, respectively.

2.2.2 Sn-Fe_2O_3-X

MOF-derived Sn-Fe_2O_3-X ($X = 0, 2, 4, 6, 8$) were obtained by annealing the Fe-MIL-88B-NH_2-Sn-X at 500 °C for 120 min with a heating rate of 2 °C min^{-1} in a muffle furnace under an air atmosphere.

2.2.3 Gas Sensing Performance

Alumina substrate gas sensor and MEMS gas sensor were used for gas sensing testing. Detailed experimental procedures and methods are exhibited in the Supporting Information.

3 Results and Discussion

3.1 Synthesis and Characterizations of Sn-Fe_2O_3-X

As illustrated in Fig. 1a, the atomically doped Sn sites in porous α-Fe_2O_3 were prepared through two steps, including the pre-substitution of Fe nodes with Sn atoms followed by oxidative annealing in air. During the crystallization process of Fe-based MOF (Fe-MIL-88B-NH_2), Sn ions were in situ trapped by the organic ligands, which also served as the molecular fences to spatially separate those Sn atoms. Different molar ratios of Sn to Fe were prepared, and the obtained samples were denoted as Fe-MIL-88B-NH_2-Sn-X ($X = 0, 2, 4, 6, 8$). After annealing in air, these materials transform into porous Fe_2O_3 with the immobilized Sn atoms (denoted as Sn-Fe_2O_3-X, $X = 0, 2, 4, 6, 8$). The X-ray diffraction (XRD) patterns of as-synthesized Fe-MIL-88B-NH_2-Sn-X (Fig. S1) show that Fe-MIL-88B-NH_2-Sn-0 matches well with the simulated results of the MIL-88B structure in the hexagonal space group of $P6_3/mmc$ [25]. Moreover, the MIL-88B structure remained almost unchanged after the introduction of Sn ions, suggesting that Sn ions did not significantly affect the crystallization process of Fe-MIL-88B-NH_2 [26]. Nevertheless, compared to Fe-MIL-88B-NH_2-Sn-0, the (101) diffraction peaks for Sn-doped MOF shift to a lower angle, and the shift degree is positively related to the addition of an amount of Sn ions. The gradually increased interplanar spacing of Fe-MIL-88B-NH_2-Sn-X could be attributed to the successful substitution of Fe nodes by Sn atoms with a larger ionic radius [27]. The transmission electron microscopy (TEM) image in Fig. 1b shows that Fe-MIL-88B-NH_2-Sn-0 has a spindle shape with average dimensions of 600 nm in length and 100 nm in width. From Figs. 1c and S2, it can be found that as the concentration of Sn ions increases, the morphology of the MOF changes from an elongated spindle shape to a stubby form. This transformation mainly originates from the altered nucleation behaviors of MOF crystals under the influence of Sn atoms [28].

Thermogravimetric analysis–derivative thermogravimetry (TGA-DTG) results (Fig. S3) confirm the complete transformation of MOF to MOS after annealing above 500 °C. The contents of Sn and Fe of Sn-Fe_2O_3-X were measured by inductively coupled plasma optical emission spectroscopy (ICP-OES) (Table S1), which are consistent with those in original Fe-MIL-88B-NH_2-Sn-X samples. The TEM images of Sn-Fe_2O_3-X (Figs. 1d and S4) clearly show the formation of the porous entities composed of several nanoparticles, corresponding to the formation of porous MOS. Besides, the morphology of Fe_2O_3 and Sn-Fe_2O_3-X ($X = 2, 4, 6, 8$) did not significantly alter, suggesting the good compatibility of the synthesis strategy. The nitrogen adsorption–desorption isotherms of Sn-Fe_2O_3-X exhibit typical IV curves, indicating

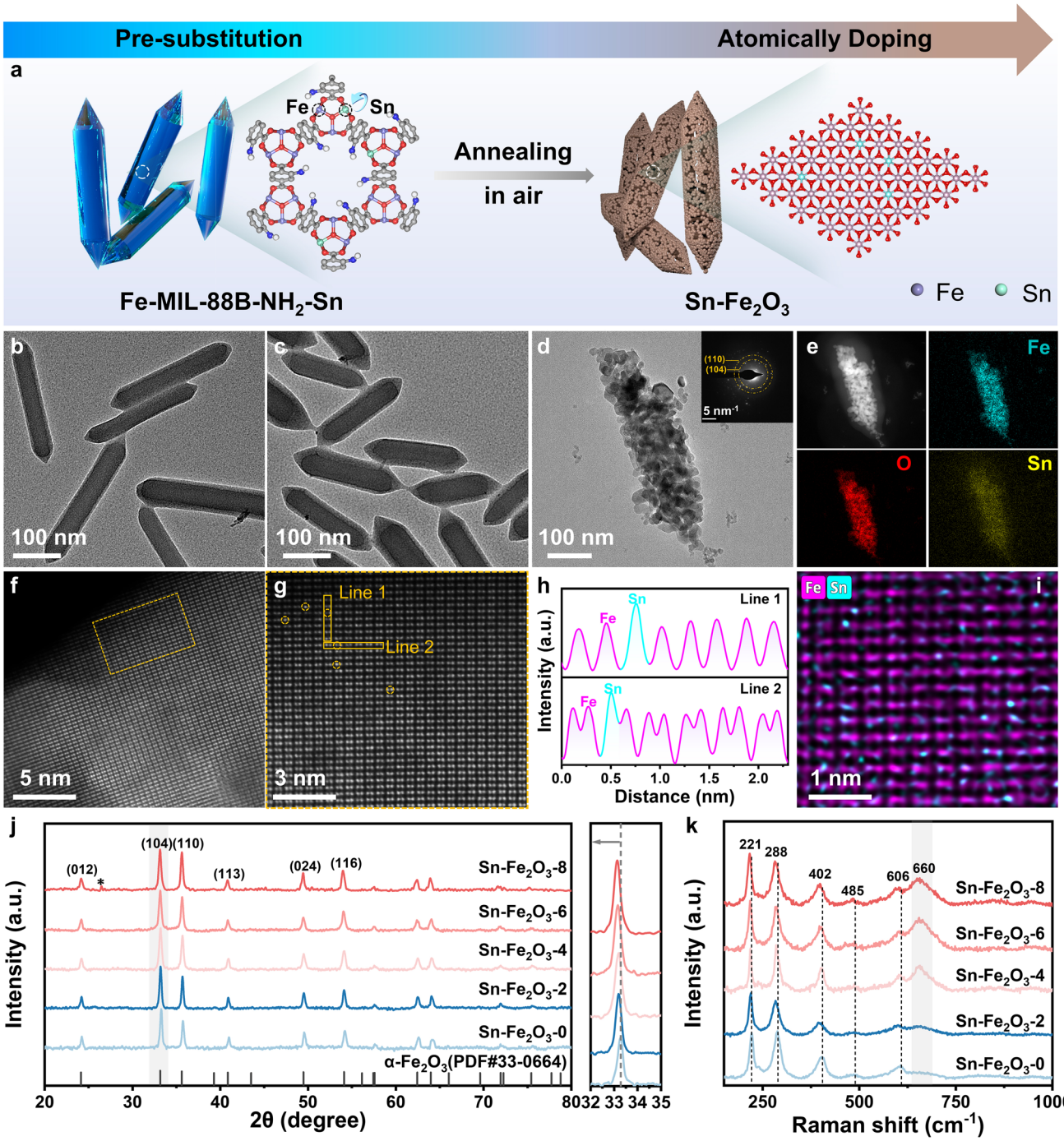


Fig. 1 Characterization of Sn-Fe_2O_3-X. **a** Schematic of synthesis procedures to atomically doping Sn sites in α-Fe_2O_3. TEM images of **b** Fe-MIL-88B-NH_2-Sn-0, **c** Fe-MIL-88B-NH_2-Sn-6. **d** TEM image of Sn-Fe_2O_3-6, along with SAED pattern (inset) and corresponding **e** HADDF-STEM image and EDX elemental mapping. **f**, **g** AC-HAADF-STEM images of Sn-Fe_2O_3-6. **h** Two profile lines were obtained from HAADF intensity analysis as labeled in **g**. **i** Atomic-resolution STEM-EDX elemental mapping for Fe, Sn in Sn-Fe_2O_3-6. **j** XRD patterns of Sn-Fe_2O_3-X. **k** Raman spectrum of Sn-Fe_2O_3-X

© The authors
https://doi.org/10.1007/s40820-025-01770-9

the presence of mesopores in the Sn-Fe_2O_3-X skeleton (Fig. S5a). The BET surface areas for Sn-Fe_2O_3-0, Sn-Fe_2O_3-2, Sn-Fe_2O_3-4, Sn-Fe_2O_3-6, and Sn-Fe_2O_3-8 were 50.7, 55.2, 61.5, 63.1, and 48.8 $m^2\ g^{-1}$, respectively. Pore size distribution analysis revealed that all of the samples had a pore size of approximately 20 nm (Fig. S5b). The above results demonstrate that the MOF derivatives have a large specific area and extensive mesoporous structure, which facilitates the interactions between sensing material and gas molecules [29]. The selected area electron diffraction (SAED) pattern of Sn-Fe_2O_3-6 (inset in Fig. 1d) shows two distinct diffraction rings that could be indexed to the (104) and (110) crystalline planes of α-Fe_2O_3. These results further confirm the transformation of Fe-based MOF into α-Fe_2O_3 during the annealing process. Furthermore, the corresponding energy-dispersive X-ray (EDX) elemental mapping images (Fig. 1e) for Sn-Fe_2O_3-6 reveal the homogeneous distribution of Fe, O, and Sn elements throughout the entire porous entity. No large Sn nanoparticles or nanoclusters were observed. To further unravel the atomic distribution of Sn atoms in α-Fe_2O_3, atomic-resolution high-angle annular dark-field scanning transmission electron microscopy (HAADF-STEM) measurements were conducted. As illustrated in the HAADF-STEM images (Fig. 1f, g) and corresponding linear intensity profiles (Fig. 1h), the Sn atoms appear brighter than the surrounding Fe and O atoms due to their higher atomic number, which definitively identifies the atomical dispersion of Sn atoms within α-Fe_2O_3. This observation is supported by the merged atomic-resolution STEM-EDX elemental mapping images of Fe and Sn atoms (Figs. 1i and S6), which show that the majority of Sn atoms (cyan dots) are located at the positions belonging to Fe lattice atoms (purple dots), suggesting that the introduced Sn atoms mainly exist in the form of occupying Fe lattice sites.

XRD patterns of Sn-Fe_2O_3-X show characteristic diffraction peaks corresponding to α-Fe_2O_3 (PDF#33–0664, Fig. 1j). The diffraction peaks of Sn-Fe_2O_3-X present a gradual shift to a lower angle with the increase in Sn contents, which is in good agreement with the incorporation of Sn into the α-Fe_2O_3 lattice. Most importantly, no observable Sn crystal could be detected, which excludes the presence of Sn nanoparticles. Besides, a weak diffraction peak at 26° corresponding to the SnO_2 (110) can be discerned for Sn-Fe_2O_3-8 sample, indicating that excessive Sn in MOF precursors would agglomerate and form Sn-related crystalline phase during the annealing process. Raman spectra of Sn-Fe_2O_3-X show two distinct vibrational modes of A_{1g} (221 and 485 cm^{-1}) and E_g (288, 402, and 606 cm^{-1}) (Fig. 1k), which are typical characters of hematite phase [30]. With the increase in Sn content, these peaks exhibit a slight redshift, indicating the weakening of the O–M–O bond. In addition, the Raman peak at 660 cm^{-1} originated from the disorder within the hematite crystal lattice and shows an increased intensity with the addition of Sn, again verifying the doping of Sn atoms into the α-Fe_2O_3 lattice [31, 32].

X-ray photoelectron spectroscopy (XPS) measurements were carried out to investigate the elemental compositions and valence states of Sn-Fe_2O_3-X. The Fe 2*p* regions (Fig. 2a) can be fitted into two pairs of characteristic peaks, indicating the coexistence of Fe (II) ($2p_{3/2}$ at 710.10 eV and $2p_{1/2}$ at 723.50 eV) and Fe (III) ($2p_{3/2}$ at 711.5 eV and $2p_{1/2}$ at 725.42 eV). Notably, the ratio of Fe^{2+} is positively correlated with Sn contents. For example, the ratio of Fe^{2+} in Sn-Fe_2O_3-6 (45.1%) is much higher than that of Sn-Fe_2O_3-0 (27.3%) (Table S2), presumably due to the electron donor from the Sn atom to the neighboring Fe atom through the O bridge [33]. In high-resolution Sn 3*d* XPS spectra, two sets of doublet peaks were observed at 494.6 and 486.2 eV (Fig. 2b), which could be attributed to $3d_{3/2}$ and $3d_{5/2}$ peaks of Sn^{4+}, respectively. Similarly, the asymmetric peaks of O 1*s* could be well fitted into three components (529.8, 531.3, and 532.4 eV), corresponding to the lattice oxygen (O_L), oxygen vacancy (O_V), and surface-chemisorbed oxygen (O_C), respectively (Fig. 2c) [34]. The detailed fitting information for Fe 2*p* and O 1*s* XPS spectra is provided in Table S2. Notably, the ratio of O_V increases with the introduction of Sn, along with the increase in Fe^{2+} sites, which implies that atomically doping Sn significantly impacts the electronic structure of α-Fe_2O_3. The existence of Ov is also confirmed by the electron paramagnetic resonance (EPR) spectra (Fig. S7), where all Sn-Fe_2O_3-X samples display a symmetric signal at $g = 2.005$, attributed to the free electrons trapped in O_V [35]. Furthermore, the photoluminscence spectrum (PL) of Sn-Fe_2O_3-X is tested in Fig. S8. The two peaks at around 460 and 470 nm correspond to the emission of the oxygen vacancy [36]. With the incorporation of Sn atoms, the Sn-Fe_2O_3-X displayed lower PL intensity, demonstrating the suppressed electron–hole combination [37].

Synchrotron radiation-based X-ray absorption spectroscopy (XAS) technique, including X-ray absorption near edge structure (XANES) and extended X-ray absorption fine structure (EXAFS), was further exploited to probe the

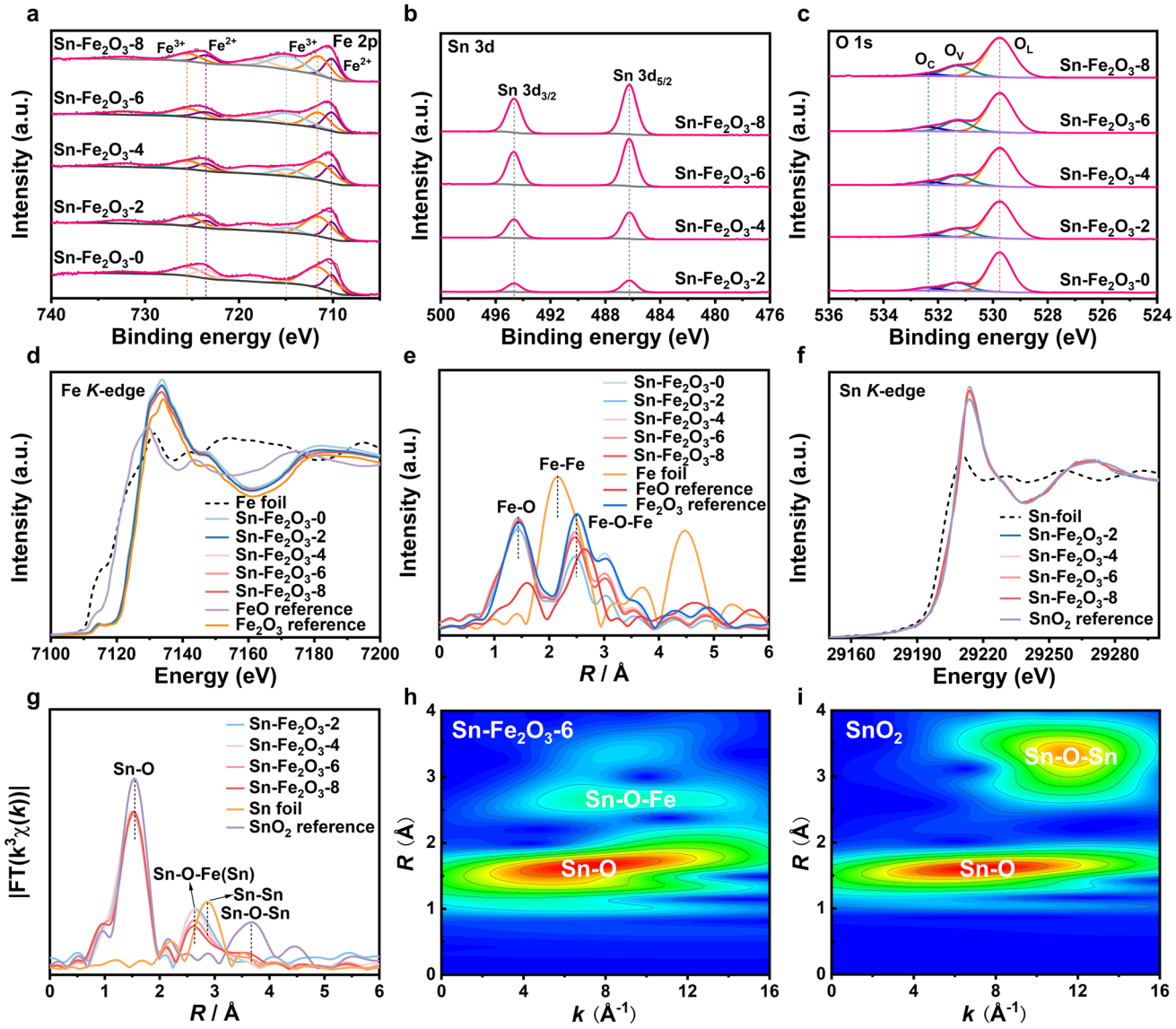


Fig. 2 Chemical state and coordination structure of Sn-Fe_2O_3-X. High-resolution XPS spectra of **a** Fe 2*p*, **b** Sn 3*d*, and **c** O 1*s*. **d** Normalized Fe *K*-edge XANES spectra of Sn-Fe_2O_3-X, Fe foil, FeO, and Fe_2O_3 reference. **e** FT k^3-weighted EXAFS spectra of Fe K-edge for Sn-Fe_2O_3-X, Fe foil, FeO, and Fe_2O_3. **f** Sn *K*-edge XANES of Sn-Fe_2O_3-X, Sn foil, and SnO_2 reference. **g** FT k^3-weighted EXAFS spectra of Sn K-edge for Sn-Fe_2O_3-X, Sn foil and SnO_2 reference. Wavelet transform of the Sn *K*-edge for the EXAFS spectra of **h** Sn-Fe_2O_3-6 and **i** SnO_2

electronic structure and local coordination environment of Fe and Sn atoms in Sn-Fe_2O_3-X. The Fe K-edge XANES spectra and corresponding first derivatives are depicted in Figs. 2d and S9. The absorption edge energies (E_0) are defined as the values of the first maxima in the first derivative spectra. In the case of Sn-Fe_2O_3-X, the E_0 of Fe lies between that of FeO and Fe_2O_3, indicating the coexistence of + 2 and + 3 oxidation states of Fe in Sn-Fe_2O_3-X. Besides, the average oxidation state of Fe can be quantitatively estimated, which is based on the fact that the edge energy is directly proportional to the average oxidation state. Figure S9 shows that the average oxidation states of Fe in Sn-Fe_2O_3-X are 2.87, 2.86, 2.84, 2.86, and 2.83, respectively. The reason is likely attributed to the existence of oxygen vacancies and the change of the local electronic structure of Fe after Sn doping. The Fe K-edge Fourier transformed (FT) EXAFS spectra for Sn-Fe_2O_3-X (Fig. 2e) exhibit two main peaks at 1.44 and 2.48 Å, which can be attributed to Fe–O and Fe–O–Fe path, respectively. Compared to the Fe_2O_3 reference, the lower FT-EXAFS intensity of the Fe–O path

© The authors
https://doi.org/10.1007/s40820-025-01770-9

for Sn-Fe_2O_3-X stems from the existence of O_V, consistent with their smaller coordination numbers of Fe–O path determined by EXAFS fitting (Fig. S11 and Table S3). Additionally, the absorption edges of Sn K-edge XANES spectra (Fig. 2f) and first derivative of Sn K-edge XANES (Fig. S10) for Sn-Fe_2O_3-X share a close energy position with that of SnO_2 reference, suggesting the Sn valences in Sn-Fe_2O_3-X were mainly + 4. The Sn EXAFS fitting results (Fig. S12 and Table S4) showed that Sn atoms with a similar coordination environment to Fe atoms remained stable. From corresponding FT-EXAFS spectra (Fig. 2g), a small peak at 2.65 Å can be discerned, which is not detected in Sn foil and SnO_2 reference but shows a similar radical distance with that of Fe–O–Fe path in α-Fe_2O_3. Furthermore, this unique path can also be observed from the Wavelet transform EXAFS (WT-EXAFS) in Fig. 2h, i. Clearly, the WT-EXAFS plot of the SnO_2 reference shows two distinct contour maximums, which can be ascribed to the contributions of Sn–O and Sn–O–Sn. In contrast, except for the contour maximum from Sn–O path, the WT-EXAFS plot of Sn-Fe_2O_3-6 shows a unique maximum that is located at a lower R- and k-position than those of Sn–O–Sn path, implying that this path originates from the scattering path between Sn atom and low-Z Fe atom. These findings demonstrate the formation of Sn–O–Fe sites, which match well with the identified doping sites of Sn atom in the α-Fe_2O_3 lattice.

3.2 Sensing Performance of Sn-Fe_2O_3-X

The contribution of atomically doping Sn sites in porous α-Fe_2O_3 sensing layer to gas sensing performance was experimentally evaluated by a series of chemiresistive sensing measurements using NO_2 as the target gas. The sensing materials were first drop-coated on prefabricated alumina substrates with interdigitated electrodes. After aging treatment, the current–voltage (I–V) curves of these devices were collected. As shown in Fig. S13, we have tested the Sn-Fe_2O_3-X based gas sensor under different temperatures to study the semiconducting properties. All samples displayed negative temperature coefficient effect, which is consistent with the characteristic of semiconductor [38]. The *I–V* curves presented in Fig. 3a show a typical symmetrical line profile, indicative of the good ohmic contact between the sensing materials layer and electrodes [39]. Generally, the sensing performance of semiconductor-based gas sensors shows an intimate correlation with the operating temperature, owing to its influence on the carrier concentration of semiconductors and the reactivity of gas molecules with the sensing materials. To identify the optimal working temperature, the Sn-Fe_2O_3-X was exposed to 1 ppm of NO_2 gas in a wide temperature range (50–200 °C). As shown in Fig. 3b, the optimal working temperature for Sn-Fe_2O_3-0 is 175 °C, while a lower optimal working temperature (150 °C) is recognized for Sn-Fe_2O_3-2, 4, 6, 8. The decrease in optimal working temperature can be attributed to the reduced activation energy of NO_2 molecules on Sn-contained sensing materials.

The dynamic response/recovery curves of the Sn-Fe_2O_3-X in response to NO_2 concentrations from 0.2 to 1 ppm are shown in Figs. 3c and S14. The Sn-Fe_2O_3-X exhibited a typical n-type response to NO_2 gas and responses of all samples increase with the increasing concentrations of NO_2 gas. For 1 ppm NO_2, the Sn-Fe_2O_3-0 (pure α-Fe_2O_3) shows a superior response value to conventional MOS-based sensors, presumably due to their structural advantages (e.g., mesopores and O_V). After the introduction of Sn, the response values are found to be dramatically improved, signifying the essential role of atomically dispersed Sn sites in the sensing process. Among them, Sn-Fe_2O_3-6 exhibits the highest response (2646.6) to 1 ppm NO_2, far surpassing Sn-Fe_2O_3-0 (349.9), Sn-Fe_2O_3-2 (1664.0), Sn-Fe_2O_3-4 (2197.3), and Sn-Fe_2O_3-8 (2147.6), denoting the optimum doping ratio of Sn for gas sensing is 6 at%. In addition, the response values of all samples display good linearity concerning NO_2 concentration (Fig. 3d), which allows for the quantitative estimation of NO_2 levels in the environment. To evaluate the response and recovery speed of the sensing materials, response/recovery time (τ_{res}/τ_{recov}) was measured at 1 ppm NO_2, as shown in Figs. 3e and S16. The τ_{res}/τ_{recov} values of Sn-Fe_2O_3-X are summarized in Table S5. Clearly, the introduction of Sn sites significantly reduces their response and recovery time to 1 ppm NO_2. The active sites (Sn–O–Fe) provide more gas adsorption and reaction sites, thereby accelerating the response process. The shortened recovery time after single-atom doping is likely due to the reduced energy barrier for NO_2 desorption at the Sn–O–Fe active sites. The presence of single Sn atoms promotes the efficient release of NO_2 molecules from the surface, thereby accelerating the recovery process. It is widely acknowledged that the practical application of NO_2 sensors is typically limited by their prolonged recovery time due to the strong oxidizing properties of the

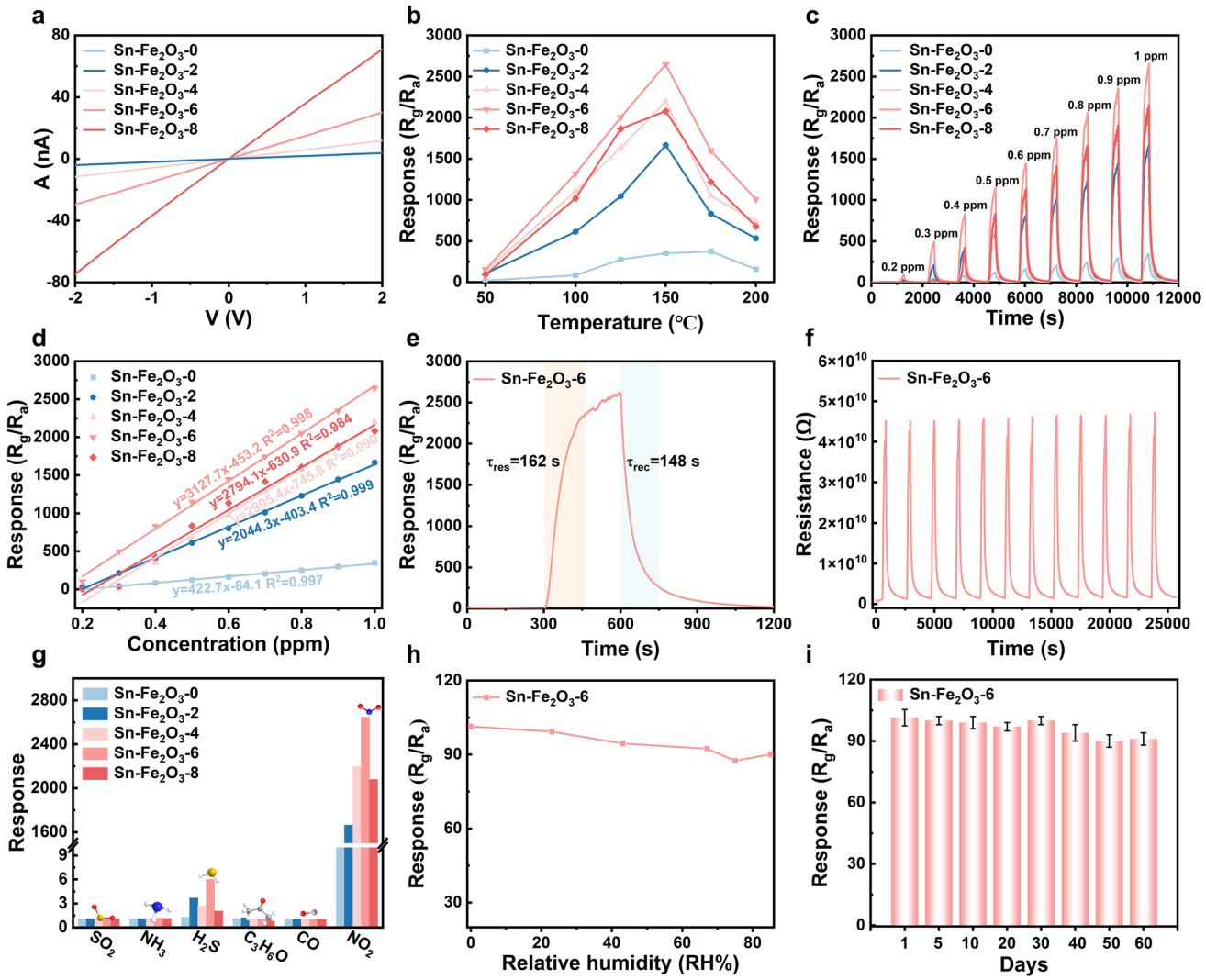


Fig. 3 Chemiresistive sensing performance of Sn-Fe_2O_3-X. **a** *I–V* curves of Sn-Fe_2O_3-X at 150 °C. **b** Response of Sn-Fe_2O_3-X to 1 ppm NO_2 at different working temperatures. **c** Dynamic response curves of Sn-Fe_2O_3-X to 0.2–1 ppm NO_2 at 150 °C. **d** Linear dependence of concentration on response. **e** Response–recover curves of Sn-Fe_2O_3-X to 1 ppm NO_2 at 150 °C. **f** Cycle reproducibility of Sn-Fe_2O_3-6 to 0.2 ppm NO_2 at 150 °C. **g** Response of Sn-Fe_2O_3-X to different gases at 150 °C. **h** The sensitivity of Sn-Fe_2O_3-6 to 0.2 ppm NO_2 in different humidity conditions **i** Long-term stability of Sn-Fe_2O_3-6 toward 0.2 ppm NO_2

NO_2 molecule, whereas the atomically dispersed Sn sites in α-Fe_2O_3 can not only enhance the sensitivity to NO_2 but also reduce its recovery time.

The repeatability of Sn-Fe_2O_3-6 was evaluated using 0.2 ppm NO_2. As displayed in Fig. 3f, the resistance of the fabricated device remained constant, showing reversible and stable characteristics during each cyclic exposure. The selectivity of Sn-Fe_2O_3-X was also investigated by exposing it to 0.2 ppm NO_2 and 1 ppm of other gases (SO_2, NH_3, H_2S, C_3H_6O, CO) at 150 °C. Figure 3g shows that the Sn-Fe_2O_3 samples exhibited superior selectivity for NO_2, demonstrating their excellent anti-interference ability. To further examine the influence of humidity on the sensitivity of Sn-Fe_2O_3-6, the response of the Sn-Fe_2O_3-6 toward 0.2 ppm NO_2 was tested under different humidity conditions. As shown in Fig. 3h, the response remains constant as humidity increases, indicating that the Sn-Fe_2O_3-6 exhibits excellent moisture resistance. Furthermore, the long-term stability of the Sn-Fe_2O_3-6 was tested under 0.2 ppm NO_2 at 150 °C, showing no significant deterioration in response over two months (Fig. 3i), further confirming its durability.

© The authors
https://doi.org/10.1007/s40820-025-01770-9

For potential commercial applications, the microelectromechanical system (MEMS)-based gas sensor was fabricated by using Sn-Fe_2O_3-6 as sensing material. The MEMS gas sensors possess various advantages, such as compact size, low power consumption, and easy integration. The structure schematic diagram of the MEMS hotplate is shown in Fig. S17a, and the hotplates were fabricated via the MEMS process, as described in Supporting Information. The sensing material was firstly coated on the testing electrodes (100×100 μm^2 in sensing area) of MEMS hotplate via an electrohydrodynamic (EHD)-based dispensing coating route by a dispensing machine. The hotplate with the sensing materials was packed in a ceramic cartridge to form a gas sensor ($3\times3\times1.3$ mm^3 in L×W×H) as shown in Fig. S17b. Figure 4a displays the response of the Sn-Fe_2O_3-6-based MEMS sensors to 20 ppb NO_2 under different heating voltages, in which the actual temperatures corresponding to different heating voltages were measured using an infrared thermometer (Figs. 4b and S18). The Sn-Fe_2O_3-6-based MEMS sensor exhibits the highest response value (2.24) at 0.7 V, corresponding to 153 °C in temperature (Fig. 4c), which is consistent with the optima working temperature of the corresponding sensing material on alumina substrate. The power consumption of the Sn-Fe_2O_3-6-based MEMS gas sensor was estimated at only 8.4 mW, which is much lower than those of commercially available MOS-based MEMS gas sensors (around 40 mW). The dynamic response/recovery curves of Sn-Fe_2O_3-6-based MEMS sensor toward ultra-low concentration of NO_2 (10–50 ppb) are shown in Fig. 4d. Obviously, the MEMS sensor exhibits an ideal response (1.58) toward 10 ppb NO_2 and displays a good linear relationship between response value and gas concentrations (Fig. 4e). These results demonstrate the potential commercialization of Sn-Fe_2O_3-6 for detecting trace amounts of NO_2 using advanced MEMS-based sensor platforms. Overall, as shown in Fig. 4f and Table S6, the MOF-derived oxygen vacancy-rich α-Fe_2O_3 with atomically dispersed Sn sites in this work exhibits superior sensitivity to NO_2 compared to most of the previously reported materials [40–48]. In addition to this, it also can test ultra-low concentration of NO_2 gas (10 ppb) instead of the theoretically calculated limit of detection.

3.3 Sensing Mechanism of Sn-Fe_2O_3-X

In metal oxide semiconductor-based gas sensors, the sensing mechanism primarily relies on changes in resistance after interaction with target gas molecules [49]. Figure 5a depicts a schematic of the gas sensing process of Sn-Fe_2O_3-X toward NO_2. Firstly, the oxygen molecules (O_2) from air atmosphere adsorb on Sn-doped Fe_2O_3, forming adsorbed oxygen species (O_2^-) [50]. The porous Fe_2O_3 with rich Ov is expected to provide abundant adsorbed oxygen species [51, 52]. As a strong oxidative electron acceptor, NO_2 has a stronger electron affinity. When exposed to NO_2 gas, these adsorbed oxygen species (mainly $O_2^-{}_{(ads)}$) interact with NO_2, or the NO_2 molecule directly adsorbs onto the sensing materials, extracting electrons from the Sn-doped Fe_2O_3 conduction band to form $NO_2^-{}_{(ads)}$ and leading to an increase in resistance, which can be measured by the external circuit of corresponding gas sensors. To investigate the effect of dispersed Sn SAs, the total density of states (DOS) of α-Fe_2O_3 before and after Sn doping were calculated (Fig. 5b). Clearly, the energy difference between the top of the valence band (VB) and the bottom of the conduction band (CB) for Sn-Fe_2O_3 is smaller than that of pure Fe_2O_3, mainly due to the disturbed charge balance caused by Sn doping. The DOS demonstrated that the introduction of single Sn atoms into the Fe_2O_3 lattice resulted in a narrowing of the bandgap. The decreased bandgap of sensing materials was also verified by the UV–vis spectra and corresponding Tauc plots, as shown in Fig. 5c, d. Therefore, the introduction of Sn atoms into Fe_2O_3 has been demonstrated to affect the local electronic structure, consequently reducing the bandgap. The reduction in the bandgap of Fe_2O_3 after Sn doping facilitates improved charge carrier mobility and enhanced surface reactivity, which collectively contribute to the superior NO_2 sensing performance at low operating temperatures. Based on the aforementioned sensing process, it can be known that the adsorption of gas molecules on sensing materials is significant to the apparent sensing performance. Furthermore, density functional theory (DFT) calculations were performed to understand the performance enhancement mechanisms introduced by atomically dispersed Sn sites. As shown in Fig. S19, two slab models, Fe_2O_3(110) and Fe_2O_3(110)-Sn ((Fe_2O_3(110) with one Fe atom replaced by Sn atom), were constructed. The charge density difference was first calculated to elucidate the charge transfer between Sn atom and Fe_2O_3. The yellow and cyan lobes in Fig. 5e represent the charge accumulation and depletion after the introduction of Sn atom. Bader charge analysis shows the net charge of Sn atom (2.22e) and surrounding O atoms (− 1.139e), implying the obvious charge transfer from Sn to the surrounding Fe_2O_3 lattice.

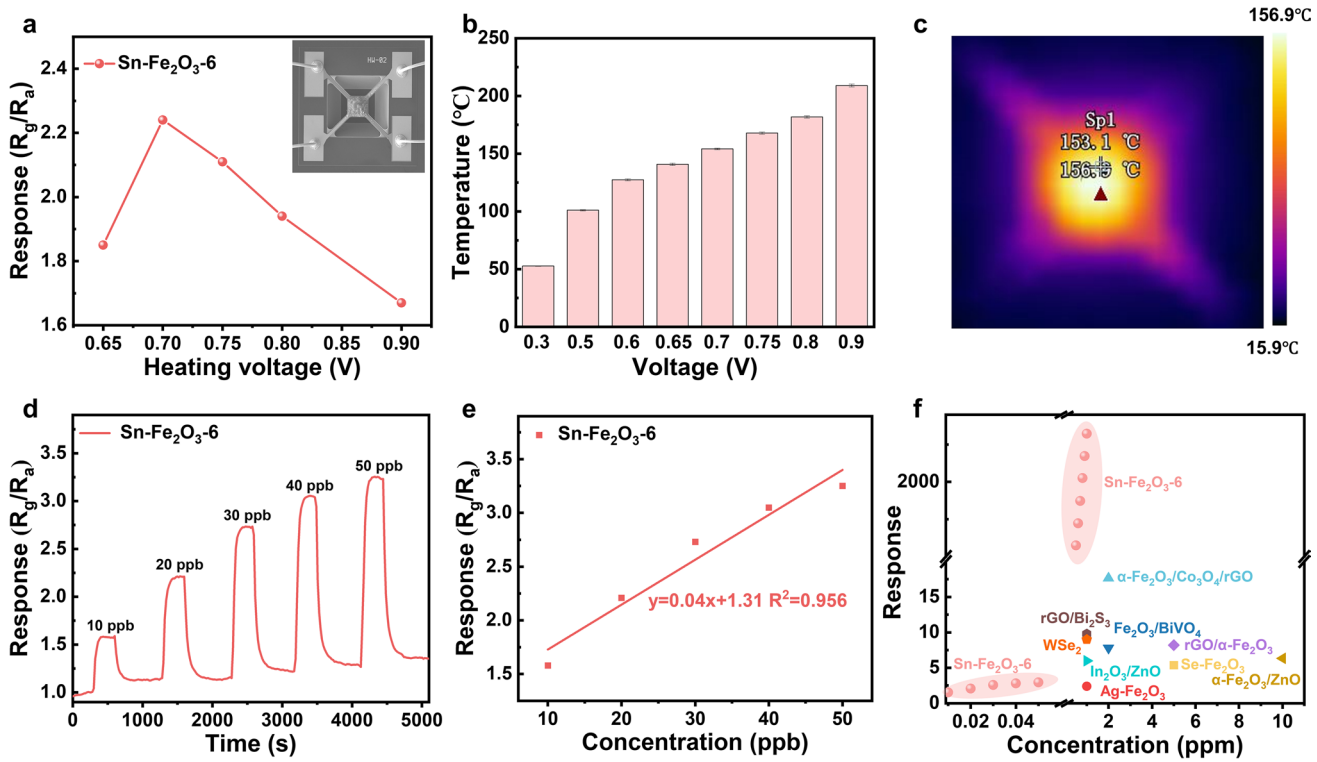


Fig. 4 Sensing performance of Sn-Fe_2O_3-6-based MEMS gas sensor. **a** The response of the Sn-Fe_2O_3-6-based MEMS gas sensor to 20 ppb NO_2 under different heating voltages along with the SEM image (inset) of sensing layer on the MEMS microheater. **b** The actual acquired temperatures under different heating voltages. **c** Infrared thermal map over the sensing area under 0.70 V. **d** Dynamic sensing characteristics of the Sn-Fe_2O_3-6-based MEMS sensor toward 10–50 ppb NO_2. **e** Correlation curve of the response of the Sn-Fe_2O_3-6-based MEMS sensor with NO_2 concentration. **f** Comparison of gas sensing performances of NO_2 sensing materials reported in recent literature and in this work

The electrons migrate from the Sn atom to the neighboring O atoms, creating a positively charged center that enhances NO_2 adsorption. This result can explain the appearance of Sn^{4+}, as detected by XPS and XANES. The adsorption energies (E_{ads}) were further calculated to evaluate the adsorption behaviors of NO_2 on Fe_2O_3 and Sn-doped Fe_2O_3. As shown in Fig. 5f, Sn and Fe atoms in Sn–O–Fe sites participate in the adsorption of NO_2 (N on Sn atom, O on Fe atom), while two Fe atoms of Fe_2O_3 function as the adsorption sites. The calculated NO_2 adsorption energy for Sn-Fe_2O_3 is −2.20 eV, which is more negative than that for pure Fe_2O_3 (−0.48 eV). It is suggested that the atomically dispersed Sn atom provides more favorable adsorption sites for NO_2 molecules, which contributes to the high response value toward NO_2. Besides, the adsorption behaviors of other gases on Sn-doped Fe_2O_3 were also investigated, as displayed in Figs. 5g, S20, and Table S7. The adsorption energies for other gases are much more positive than that for NO_2, indicating their lower adsorption intensities on Sn-doped Fe_2O_3. Overall, the atomically dispersed Sn atom within Sn-doped Fe_2O_3 plays a critical role in improving the sensitivity and selectivity of corresponding gas sensors toward NO_2, which is mainly realized by providing both favorable adsorption sites and available conductive electrons.

4 Conclusions

In this work, atomically dispersed Sn sites within porous α-Fe_2O_3 were successfully synthesized through the in situ trapping of Sn atoms during MOF crystallization and subsequent atomic dispersion during the annealing process. Comprehensive structural evidence from STEM and XAS have clearly demonstrated that Sn atoms were incorporated into the porous Fe_2O_3 matrix as atomically dispersed sites, forming Sn–O–Fe configurations. The Sn-Fe_2O_3-6-based MEMS gas sensor exhibits exceptional sensing performance toward NO_2 gas at a low operating temperature of

© The authors
https://doi.org/10.1007/s40820-025-01770-9

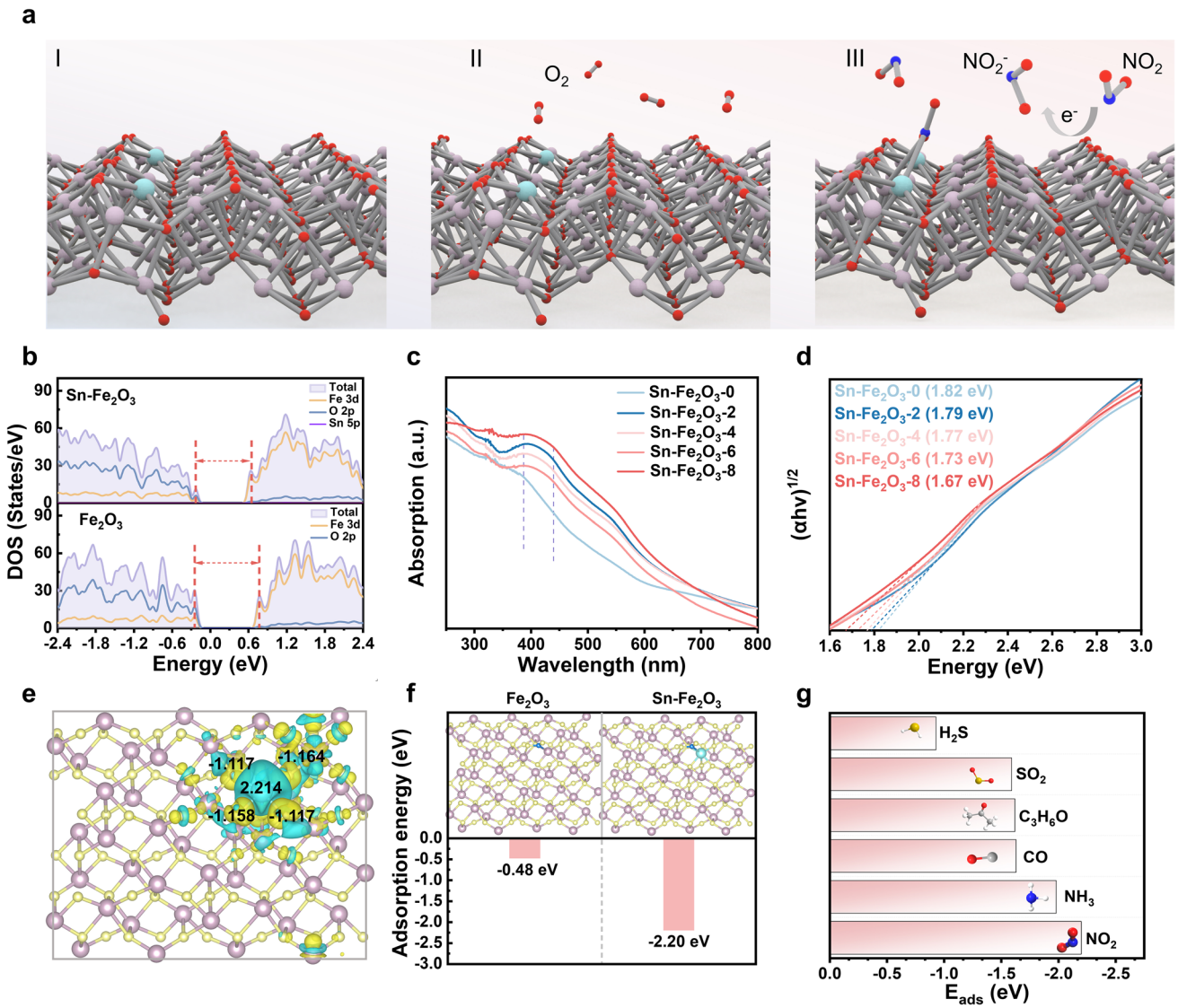


Fig. 5 Investigation of the role of Sn-single sites in sensing progress. a Sensing process diagram of Sn-Fe_2O_3 for NO_2. **b** Density of state of Fe_2O_3 and Sn-Fe_2O_3 obtained from DFT calculations. **c** UV–vis absorption spectra of Sn-Fe_2O_3-X. **d** Tauc plot according to the UV–vis absorption spectra to estimate the bandgap. **e** Charge density of Sn-Fe_2O_3 and net charge of Sn and surrounding O atoms. Charge accumulation and depletion are indicated by yellow and cyan areas, respectively. **f** Adsorption energies of NO_2 on the optimum structures of Fe_2O_3 and Sn-Fe_2O_3. **g** Adsorption energies of different gases on the optimum structure of Sn-Fe_2O_3

150 °C, achieving a high response (2646.6–1 ppm NO_2), an ultra-low detection limit (10 ppb), excellent selectivity, and long-term stability. DFT calculations revealed that the enhanced sensing performance of Sn-doped Fe_2O_3 is attributed to the specific adsorption sites and additional conductive electrons provided by atomically dispersed Sn atoms. These findings highlight the potential of atomically dispersed sites for high-performance gas sensors and offer a strategic pathway for designing advanced sensing materials for practical applications.

Acknowledgements The work was supported by the National Key Research and Development Project of China (Grant No. 2022YFB3205500), the National Natural Science Foundation of China (Grant No. 12275190, 12105201), Jiangsu Funding Program for Excellent Postdoctoral Talent (Grant No. 2024ZB723), and the Shenzhen Research Funding Program (JCYJ20230807154402004). This work was also supported by the Collaborative Innovation Center of Suzhou Nano Science & Technology, the Priority Academic Program Development of Jiangsu Higher Education Institutions (PAPD), the 111 Project, the Joint International Research Laboratory of Carbon-Based Functional Materials and Devices, and the Suzhou Key Laboratory of Functional Nano & Soft Materials

and Soochow University-Western University Centre for Synchrotron Radiation Research. The authors also thank the BL14W1, BL20U1 beamline of Shanghai Synchrotron Facilities (SSRF) for providing beamtime and support of XAS measurements.

Author Contributions Yihong Zhong contributed to investigation, experiment operation, data processing, and original draft writing. Guotao Yuan, Dequan Bao, and Yi Tao were involved in discussion and analysis. Zhenqiu Gao, Wei Zhao, Shuo Li, Yuting Yang, and Pingping Zhang contributed to data processing and analysis. Hao Zhang and Xuhui Sun were involved in conceptualization, investigation, supervision, funding acquisition, review, and editing.

Declarations

Conflict of interest The authors declare no interest conflict. They have no known competing financial interests or personal relationships that could have appeared to influence the work reported in this paper.

Open Access This article is licensed under a Creative Commons Attribution 4.0 International License, which permits use, sharing, adaptation, distribution and reproduction in any medium or format, as long as you give appropriate credit to the original author(s) and the source, provide a link to the Creative Commons licence, and indicate if changes were made. The images or other third party material in this article are included in the article's Creative Commons licence, unless indicated otherwise in a credit line to the material. If material is not included in the article's Creative Commons licence and your intended use is not permitted by statutory regulation or exceeds the permitted use, you will need to obtain permission directly from the copyright holder. To view a copy of this licence, visit http://creativecommons.org/licenses/by/4.0/.

Supplementary Information The online version contains supplementary material available at https://doi.org/10.1007/s40820-025-01770-9.

References

1. A. Sharma, S.B. Eadi, H. Noothalapati, M. Otyepka, H.-D. Lee et al., Porous materials as effective chemiresistive gas sensors. Chem. Soc. Rev. **53**(5), 2530–2577 (2024). https://doi.org/10.1039/D2CS00761D
2. B. Zong, S. Wu, Y. Yang, Q. Li, T. Tao et al., Smart gas sensors: recent developments and future prospective. Nano-Micro Lett. **17**(1), 54 (2024). https://doi.org/10.1007/s40820-024-01543-w
3. F. Zheng, H.-Y. Jiang, X.-T. Yang, J.-H. Guo, L. Sun et al., Reviews of wearable healthcare systems based on flexible gas sensors. Chem. Eng. J. **490**, 151874 (2024). https://doi.org/10.1016/j.cej.2024.151874
4. P. Wu, Y. Li, A. Yang, X. Tan, J. Chu et al., Advances in 2D materials based gas sensors for industrial machine olfactory applications. ACS Sens. **9**(6), 2728–2776 (2024). https://doi.org/10.1021/acssensors.4c00431
5. G. Verma, A. Gokarna, H. Kadiri, K. Nomenyo, G. Lerondel et al., Multiplexed gas sensor: fabrication strategies, recent progress, and challenges. ACS Sens. **8**(9), 3320–3337 (2023). https://doi.org/10.1021/acssensors.3c01244
6. M. Taheri, I.A. Deen, M. Packirisamy, M.J. Deen, Metal oxide-based electrical/electrochemical sensors for health monitoring systems. TrAC Trends Anal. Chem. **171**, 117509 (2024). https://doi.org/10.1016/j.trac.2023.117509
7. M.J. Cooper, R.V. Martin, M.S. Hammer, P.F. Levelt, P. Veefkind et al., Global fine-scale changes in ambient NO_2 during COVID-19 lockdowns. Nature **601**(7893), 380–387 (2022). https://doi.org/10.1038/s41586-021-04229-0
8. T. Xue, M. Tong, M. Wang, X. Yang, Y. Wang et al., Health impacts of long-term NO_2 exposure and inequalities among the Chinese population from 2013 to 2020. Environ. Sci. Technol. **57**(13), 5349–5357 (2023). https://doi.org/10.1021/acs.est.2c08022
9. M. Krzyzanowski, A. Cohen, Update of WHO air quality guidelines. Air Qual. Atmos. Health **1**(1), 7–13 (2008). https://doi.org/10.1007/s11869-008-0008-9
10. L.X. Ou, M.Y. Liu, L.Y. Zhu, D.W. Zhang, H.L. Lu, Recent progress on flexible room-temperature gas sensors based on metal oxide semiconductor. Nano-Micro Lett. **14**(1), 206 (2022). https://doi.org/10.1007/s40820-022-00956-9
11. S. Ma, J. Xu, Nanostructured metal oxide heterojunctions for chemiresistive gas sensors. J. Mater. Chem. A **11**(44), 23742–23771 (2023). https://doi.org/10.1039/d3ta04953a
12. Q. Li, W. Zeng, Y. Li, Metal oxide gas sensors for detecting NO_2 in industrial exhaust gas: recent developments. Sens. Actuat. B Chem. **359**, 131579 (2022). https://doi.org/10.1016/j.snb.2022.131579
13. C. Zhu, S. Fu, Q. Shi, D. Du, Y. Lin, Single-atom electrocatalysts. Angew. Chem. Int. Ed. **56**(45), 13944–13960 (2017). https://doi.org/10.1002/anie.201703864
14. Q. Zhang, J. Guan, Single-atom catalysts for electrocatalytic applications. Adv. Funct. Mater. **30**(31), 2000768 (2020). https://doi.org/10.1002/adfm.202000768
15. N. Cheng, L. Zhang, K. Doyle-Davis, X. Sun, Single-atom catalysts: from design to application. Electrochem. Energy Rev. **2**(4), 539–573 (2019). https://doi.org/10.1007/s41918-019-00050-6
16. S. Ji, Y. Chen, X. Wang, Z. Zhang, D. Wang et al., Chemical synthesis of single atomic site catalysts. Chem. Rev. **120**(21), 11900–11955 (2020). https://doi.org/10.1021/acs.chemrev.9b00818
17. Y. Chen, S. Ji, C. Chen, Q. Peng, D. Wang et al., Single-atom catalysts: synthetic strategies and electrochemical applications. Joule **2**(7), 1242–1264 (2018). https://doi.org/10.1016/j.joule.2018.06.019
18. C. Kim, H. Min, J. Kim, J.H. Moon, Boosting electrochemical methane conversion by oxygen evolution reactions on Fe–N–C single atom catalysts. Energy Environ. Sci. **16**(7), 3158–3165 (2023). https://doi.org/10.1039/D3EE00027C

19. F. Gu, Y. Cui, D. Han, S. Hong, M. Flytzani-Stephanopoulos et al., Atomically dispersed Pt (II) on WO_3 for highly selective sensing and catalytic oxidation of triethylamine. Appl. Catal. B Environ. **256**, 117809 (2019). https://doi.org/10.1016/j.apcatb.2019.117809
20. B. Feng, Z. Wang, Y. Feng, P. Li, Y. Zhu et al., Single-atom Au-functionalized mesoporous SnO_2 nanospheres for ultrasensitive detection of *Listeria monocytogenes* biomarker at low temperatures. ACS Nano **18**(34), 22888–22900 (2024). https://doi.org/10.1021/acsnano.4c03566
21. P. Wang, S. Guo, Z. Hu, L. Zhou, T. Li et al., Single-atom Cu stabilized on ultrathin $WO_{2.72}$ nanowire for highly selective and ultrasensitive ppb-level toluene detection. Adv. Sci. **10**(26), 2302778 (2023). https://doi.org/10.1002/advs.202302778
22. T. Chu, C. Rong, L. Zhou, X. Mao, B. Zhang et al., Progress and perspectives of single-atom catalysts for gas sensing. Adv. Mater. **35**(3), 2206783 (2023). https://doi.org/10.1002/adma.202206783
23. G. Lei, H. Pan, H. Mei, X. Liu, G. Lu et al., Emerging single atom catalysts in gas sensors. Chem. Soc. Rev. **51**(16), 7260–7280 (2022). https://doi.org/10.1039/d2cs00257d
24. M.-H. Pham, G.-T. Vuong, A.-T. Vu, T.-O. Do, Novel route to size-controlled Fe-MIL-88B-NH_2 metal-organic framework nanocrystals. Langmuir **27**(24), 15261–15267 (2011). https://doi.org/10.1021/la203570h
25. C. Serre, F. Millange, S. Surblé, G. Férey, A route to the synthesis of trivalent transition-metal porous carboxylates with trimeric secondary building units. Angew. Chem. Int. Ed. **43**(46), 6285–6289 (2004). https://doi.org/10.1002/anie.200454250
26. V. Pascanu, A. Bermejo Gómez, C. Ayats, A.E. Platero-Prats, F. Carson et al., Double-supported silica-metal–organic framework palladium nanocatalyst for the aerobic oxidation of alcohols under batch and continuous flow regimes. ACS Catal. **5**(2), 472–479 (2015). https://doi.org/10.1021/cs501573c
27. W. Tian, J. Han, L. Wan, N. Li, D. Chen et al., Enhanced piezocatalytic activity in ion-doped SnS_2 *via* lattice distortion engineering for BPA degradation and hydrogen production. Nano Energy **107**, 108165 (2023). https://doi.org/10.1016/j.nanoen.2023.108165
28. J. Łuczak, M. Kroczewska, M. Baluk, J. Sowik, P. Mazierski et al., Morphology control through the synthesis of metal-organic frameworks. Adv. Colloid Interface Sci. **314**, 102864 (2023). https://doi.org/10.1016/j.cis.2023.102864
29. H. Yuan, N. Li, W. Fan, H. Cai, D. Zhao, Metal-organic framework based gas sensors. Adv. Sci. **9**(6), 2104374 (2022). https://doi.org/10.1002/advs.202104374
30. J. Deng, S. Cai, M. Gao, J.-Y. Hasegawa, H. Yao et al., Crystal-in-amorphous vanadate catalysts for universal poison-resistant elimination of nitric oxide. ACS Catal. **13**(18), 12363–12373 (2023). https://doi.org/10.1021/acscatal.3c02571
31. A.M. Jubb, H.C. Allen, Vibrational spectroscopic characterization of hematite, maghemite, and magnetite thin films produced by vapor deposition. ACS Appl. Mater. Interfaces **2**(10), 2804–2812 (2010). https://doi.org/10.1021/am1004943
32. A.K. Bhunia, B. Mahata, B. Mandal, P.K. Guha, S. Saha, Emerging 2D nanoscale metal oxide sensor: semiconducting CeO_2 nano-sheets for enhanced formaldehyde vapor sensing. Nanotechnology **35**(45), 455501 (2024). https://doi.org/10.1088/1361-6528/ad6e8b
33. W. Chen, S. Yang, H. Liu, F. Huang, Q. Shao et al., Single-atom Ce-modified α-Fe_2O_3 for selective catalytic reduction of NO with NH_3. Environ. Sci. Technol. **56**(14), 10442–10453 (2022). https://doi.org/10.1021/acs.est.2c02916
34. L. Zhao, C. Yu, C. Xin, Y. Xing, Z. Wei et al., Increasing the catalytic activity of Co_3O_4 *via* boron doping and chemical reduction for enhanced acetone detection. Adv. Funct. Mater. **34**(18), 2314174 (2024). https://doi.org/10.1002/adfm.202314174
35. L. Gui, Z. Wang, K. Zhang, B. He, Y. Liu et al., Oxygen vacancies-rich $Ce_{0.9}Gd_{0.1}O_{2-\delta}$ decorated $Pr_{0.5}Ba_{0.5}Co_{O3-\delta}$ bifunctional catalyst for efficient and long-lasting rechargeable Zn-air batteries. Appl. Catal. B Environ. **266**, 118656 (2020). https://doi.org/10.1016/j.apcatb.2020.118656
36. B. Mandal, A.K. Bhunia, B. Mahata, S. Roy, S. Acharyya et al., Defect-rich SnO_{2-x} polydisperse spheres toward the detection of vehicle-emitted category NO_2 gas. IEEE Sens. J. **24**(17), 27183–27190 (2024). https://doi.org/10.1109/JSEN.2024.3429543
37. H. Xie, Y. Song, Y. Jiao, L. Gao, S. Shi et al., Engineering surface passivation and hole transport layer on hematite photoanodes enabling robust photoelectrocatalytic water oxidation. ACS Nano **18**(7), 5712–5722 (2024). https://doi.org/10.1021/acsnano.3c11638
38. A.K. Bhunia, B. Mandal, P.K. Guha, Efficient ethanol sensor based on vertically aligned ZnO nanorods on radio frequency sputtered ZnO/Pt/SiO_2/Si substrate. Phys. Status Solidi RRL **19**(3), 2400285 (2025). https://doi.org/10.1002/pssr.202400285
39. Y. Hong, L. Wei, Q. Zhang, Z. Deng, X. Liao et al., A broad-spectrum gas sensor based on correlated two-dimensional electron gas. Nat. Commun. **14**(1), 8496 (2023). https://doi.org/10.1038/s41467-023-44331-7
40. T. Liang, Y. Li, X. Zhang, H. Bao, F. Li et al., Selenium-doped hematite (α-Fe_2O_3) hollow nanorods for highly sensitive and selective detection of trace NO_2. J. Mater. Chem. C **13**(13), 6660–6668 (2025). https://doi.org/10.1039/d4tc05464d
41. A. Mirzaei, K. Janghorban, B. Hashemi, M. Bonyani, S.G. Leonardi et al., A novel gas sensor based on Ag/Fe_2O_3 core-shell nanocomposites. Ceram. Int. **42**(16), 18974–18982 (2016). https://doi.org/10.1016/j.ceramint.2016.09.052
42. L. Sun, J. Sun, K. Zhang, X. Sun, S. Bai et al., rGO functionalized α-Fe_2O_3/Co_3O_4 heterojunction for NO_2 detection. Sens. Actuat. B Chem. **354**, 131194 (2022). https://doi.org/10.1016/j.snb.2021.131194
43. S.L. Bai, K. Tian, H. Fu, Y.J. Feng, R.X. Luo et al., Novel α-Fe_2O_3/$BiVO_4$ heterojunctions for enhancing NO_2 sensing properties. Sens. Actuat. B-Chem. **268**, 136–143 (2018). https://doi.org/10.1016/j.snb.2018.03.173

44. B. Zhang, G. Liu, M. Cheng, Y. Gao, L. Zhao et al., The preparation of reduced graphene oxide-encapsulated α-Fe_2O_3 hybrid and its outstanding NO_2 gas sensing properties at room temperature. Sens. Actuat. B Chem. **261**, 252–263 (2018). https://doi.org/10.1016/j.snb.2018.01.143
45. Y.-C. Liang, Y.-W. Hsu, Enhanced sensing ability of brush-like Fe_2O_3-ZnO nanostructures towards NO_2 gas *via* manipulating material synergistic effect. Int. J. Mol. Sci. **22**(13), 6884 (2021). https://doi.org/10.3390/ijms22136884
46. C. Han, X. Li, Y. Liu, X. Li, C. Shao et al., Construction of In_2O_3/ZnO yolk-shell nanofibers for room-temperature NO_2 detection under UV illumination. J. Hazard. Mater. **403**, 124093 (2021). https://doi.org/10.1016/j.jhazmat.2020.124093
47. Y. Yang, M. Zhu, H. Zhang, B. Wang, C. Chen et al., Room temperature gas sensor based on rGO/Bi_2S_3 heterostructures for ultrasensitive and rapid NO_2 detection. Chem. Eng. J. **490**, 151872 (2024). https://doi.org/10.1016/j.cej.2024.151872
48. G.-C. Lu, X.-H. Liu, W. Zheng, J.-Y. Xie, Z.-S. Li et al., UV-activated single-layer WSe_2 for highly sensitive NO_2 detection. Rare Met. **41**(5), 1520–1528 (2022). https://doi.org/10.1007/s12598-021-01899-7
49. H. Ji, W. Zeng, Y. Li, Gas sensing mechanisms of metal oxide semiconductors: a focus review. Nanoscale **11**(47), 22664–22684 (2019). https://doi.org/10.1039/c9nr07699a
50. G.-L. Chen, M.-S. Lv, L.-L. Sui, Z.-P. Deng, Y.-M. Xu et al., Low-temperature and dual-sensing NO_2/dimethylamine sensor based on single-crystal WO_3 nanoparticles-supported sheets synthesized by simple pyrolysis of spoiled WCl_6 powder. Chem. Eng. J. **464**, 142528 (2023). https://doi.org/10.1016/j.cej.2023.142528
51. M. Al-Hashem, S. Akbar, P. Morris, Role of oxygen vacancies in nanostructured metal-oxide gas sensors: a review. Sens. Actuat. B Chem. **301**, 126845 (2019). https://doi.org/10.1016/j.snb.2019.126845
52. C. Zhang, G. Liu, X. Geng, K. Wu, M. Debliquy, Metal oxide semiconductors with highly concentrated oxygen vacancies for gas sensing materials: a review. Sens. Actuat. A Phys. **309**, 112026 (2020). https://doi.org/10.1016/j.sna.2020.112026

Publisher's Note Springer Nature remains neutral with regard to jurisdictional claims in published maps and institutional affiliations.

© The authors https://doi.org/10.1007/s40820-025-01770-9